

Bistable spin-crossover in a new series of $[\text{Fe}(\text{BPP-R})_2]^{2+}$ (BPP = 2,6-bis(pyrazol-1-yl)pyridine; R = CN) complexes[†]

Kuppusamy Senthil Kumar,^{a,b,*} Nicolas Del Giudice,^a Benoît Heinrich,^a Laurent Douce,^a and Mario Ruben^{a,b,d,*}

^aInstitut de Physique et Chimie des Matériaux de Strasbourg (IPCMS), CNRS-Université de Strasbourg, 23, rue du Loess, BP 43, 67034 Strasbourg cedex 2, France.

^bInstitute of Nanotechnology (INT), Karlsruhe Institute of Technology (KIT), Hermann-von-Helmholtz-Platz 1, 76344, Eggenstein-Leopoldshafen, Germany.

^cService de Radiocristallographie, Fédération de Chimie Le Bel FR2010 CNRS-Université de Strasbourg, 1 rue Blaise Pascal, BP 296/R8, 67008 Strasbourg cedex, France.

^dInstitute of Quantum Materials and Technologies (IQMT), Karlsruhe Institute of Technology (KIT), Hermann-von-Helmholtz-Platz 1, 76344, Eggenstein-Leopoldshafen, Germany.

*e-mail: kavinsenthil82@gmail.com; mario.ruben@kit.edu

[†]Electronic supplementary information (ESI) is available. Synthesis and characterization details of ligand (**L**) and complexes **1a-d** and **2**; crystallographic parameters of complex **1c** (CCDC 1961768); electronic absorption spectra of the ligand and complexes; $\chi_M T$ versus T and $d(\chi_M T)/dT$ versus T plots of complexes **1b**, **1c**, and **1d**; differential scanning calorimetric (DSC) analyses of complexes **1c** and **1d**, see DOI:

*A new series of iron(II) complexes— $[\text{Fe}(\text{BPP-CN})_2](X)_2$, $X = \text{BF}_4$ (**1a-d**) or ClO_4 (**2**)—belonging to the $[\text{Fe}(\text{BPP-R})_2]^{2+}$ (BPP = 2,6-bis(pyrazol-1-yl)pyridine) family of complexes showed abrupt and hysteretic, that is, bistable, spin-crossover (SCO) characteristics. Among the complexes, the lattice solvent-free complex **2** showed a stable and complete SCO ($T_{1/2} = 241$ K) with a thermal hysteresis width (ΔT) of 28 K, the widest ΔT so far reported for a $[\text{Fe}(\text{BPP-R})_2](X)_2$ family of complex, showing abrupt SCO. The reproducible and bistable SCO shown by the relatively simple $[\text{Fe}(\text{BPP-CN})_2](X)_2$ series of molecular complexes is encouraging to pursue $[\text{Fe}(\text{BPP-R})_2]^{2+}$ systems for the realization of technologically relevant SCO complexes.*

The captivating phenomenon of spin-crossover (SCO)^{1–10} exhibited by molecular systems composed of first-row transition metal ions—featuring d^4 – d^7 electronic configurations—is of significance in chemistry,^{11–20} materials science,^{16,21–25} biology,²⁶ and geology.²⁷ In chemistry and materials science, the synthesis and structure-property relationship studies of SCO active molecular complexes are actively pursued to develop molecule-based switching and memory architectures.^{23,28} Molecular complexes featuring abrupt and hysteretic spin-state switching, that is, bistable SCO, are especially suited for switching and memory applications.^{29–32} Iron(II) complexes composed of all nitrogen-based BPP (BPP = 2,6-bis(pyrazol-1-yl)pyridine) ligand systems are a prominent example of SCO complexes exhibiting bistable SCO.^{33–38} Various parameters, for example, intermolecular interactions, molecular packing, electronic substituent effects, governing the occurrence and nature of SCO—gradual, abrupt, and bistable—in $[\text{Fe}(\text{BPP-R})]^{2+}$ complexes have been elucidated.¹³ Although some $[\text{Fe}(\text{BPP-R})]^{2+}$ complexes show bistable SCO, the thermal hysteresis width (ΔT) associated with the spin-state switching of the complexes are well below the value of $\Delta T \geq 40$ K proposed suitable for technological applications.²¹

A systematic molecular-engineering-based approach and a clear elucidation of factors governing SCO are the need of the hour to obtain $[\text{Fe}(\text{BPP-R})]^{2+}$ complexes, featuring wide ΔT .³⁹ Despite having some understanding on structural features governing SCO in the $[\text{Fe}(\text{BPP-R})]^{2+}$ complexes, a pre-synthesis design of $[\text{Fe}(\text{BPP-R})]^{2+}$ complexes capable of showing $\Delta T \geq 40$ K is still marred by the complex interplay between the SCO event and various structural parameters governing it. Therefore, the realization of technologically useful $[\text{Fe}(\text{BPP-R})]^{2+}$ complexes could only be achieved by systematically varying the R group on $[\text{Fe}(\text{BPP-R})]^{2+}$ complexes on an experimental basis. The recently reported $[\text{Fe}(\text{BPP-COOEt})_2](\text{ClO}_4)_2 \cdot \text{CH}_3\text{CN}$ complex is a prominent example of such an effort. The complex has shown a thermal hysteresis width of 101 K ($T_{1/2} = 233$ K) for the first HS→LS→HS cycle, the highest ΔT so far reported for an $[\text{Fe}(\text{BPP-R})]^{2+}$ complex; however, the SCO of the complex was not stable in the subsequent cycles.⁴⁰ This shortcoming prompted us to search for a new series of $[\text{Fe}(\text{BPP-R})]^{2+}$ complexes, which could exhibit stable and bistable SCO characteristics. Consequently, we have designed and synthesized a new ligand—2,6-bis(1H-pyrazol-1-yl)pyridine-4-carbonitrile (BPP-CN)—featuring a CN substituent at the 4-position of the central pyridine ring of the BPP skeleton. In this communication, we report on the bistable SCO characteristics of $[\text{Fe}(\text{BPP-CN})_2](\text{X})_2$, X = BF_4 (**1a–d**) or ClO_4 (**2**) series of complexes.

The BPP-CN ligand (**L**) was synthesized from the precursor 4-iodo-2,6-bis(1H-pyrazol-1-yl)pyridine (**I-BPP**) by performing the classical Rosenmund-von Braun reaction⁴¹ as shown in Chart 1. Addition of solid $[\text{Fe}(\text{BF}_4)_2] \cdot 6\text{H}_2\text{O}$ to a clear acetonitrile (ACN) solution of the ligand followed by gentle swirling resulted in the formation of a homogenous solution, which was allowed to stand undisturbed for a week. This procedure resulted in the formation of orange microcrystalline form of $[\text{Fe}(\text{BPP-CN})_2](\text{BF}_4)_2$ —**1a**—at the

bottom of the reaction vial. Slow diffusion of diethyl ether (Et_2O) into the orange filtrate, obtained after the separation of **1a**, yielded orange plate-like (**1b**) and red rod-like (**1c**·ACN, referred to as **1c** for simplicity) crystalline forms of $[\text{Fe}(\text{BPP-CN})_2](\text{BF}_4)_2$; the crystalline materials were manually separated for further analysis. X-ray diffraction studies of the red rod-like crystals confirmed the formation of the expected iron(II) complex as shown in Chart 1. On the other hand, the attempted structure determination of the orange plate-like crystals was not fruitful due to the bad quality of the crystals.

To analyse the role of crystallinity on the SCO characteristics, powder form of $[\text{Fe}(\text{BPP-CN})_2](\text{BF}_4)_2$ —**1d**—was prepared using a 1:1 acetonitrile/dichloromethane solvent mixture.

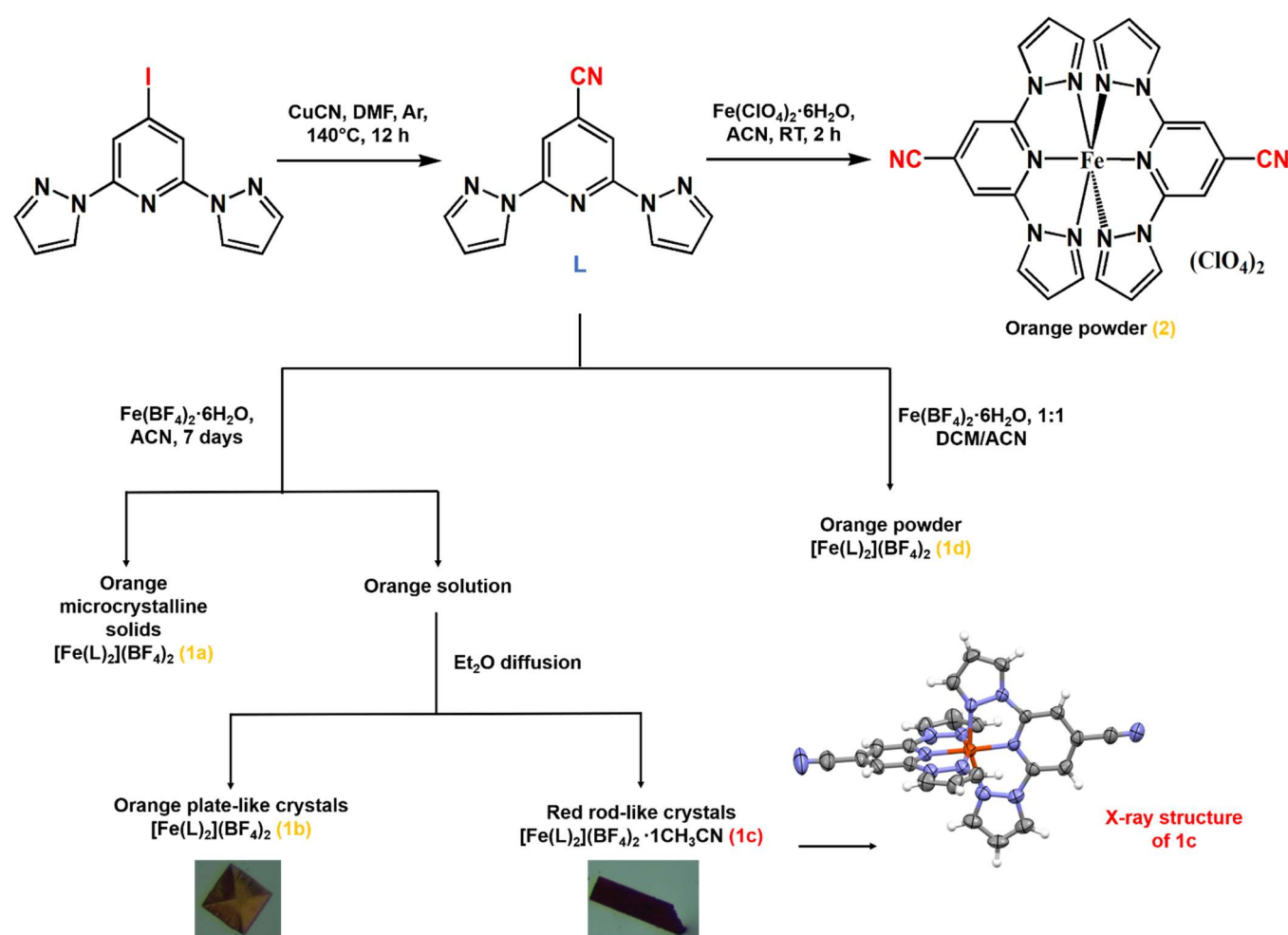


Chart 1. Synthetic step involved in the preparation of **L** and the methodology devised to prepare complexes **1a-d** and complex **2**. The X-ray structure of complex **1c** is shown at the bottom of the chart. Complex **1c** crystallised with a lattice ACN solvent molecule (omitted for clarity in the picture) in the $P2_12_12_1$ space group, belonging to the orthorhombic crystal system. The average bond lengths and angular parameters (Table S1) associated with the X-ray structure of **1c** indicates the LS-state of it at 300 K. In the crystal lattice, the complex cations were organized in a non-terpyridine embrace packing pattern;^{13,42} see figure S1

and S2 for more details. The UV-vis absorption spectra of **L**, **1a**, and **2** are shown in figure S3, and the corresponding parameters are listed in table S2.

Remarkably, rapid precipitation of complex **2** occurred after the addition of solid $[\text{Fe}(\text{ClO}_4)_2] \cdot 6\text{H}_2\text{O}$ to a clear ACN solution of **L**; the complex was collected by filtration after stirring the heterogeneous reaction mixture for two hours under ambient conditions. Our attempts to crystallise the complex from the filtrate by diffusing Et_2O were not successful.

All the complexes reported in this study are SCO active, as inferred from the variable temperature magnetic measurements. Complexes **1a**, **1b**, **1d**, and **2** showed reproducible, abrupt, and hysteretic SCO, whereas complex **1c** showed lattice solvent dependent SCO, which varied with cycle. Complexes **1d** and **2** showed one-step SCO, facilitating the estimation of ΔT straightforward from the peak positions of $d(\chi_M T)/dT$ (first derivative) versus T plots. On the contrary, the SCO of complexes **1a-c** occurred with plateau-like features, making the estimation of ΔT less straightforward. To address this issue, critical transition temperatures associated with the cooling ($T_{C\downarrow}$) and heating ($T_{C\uparrow}$) branches of $\chi_M T$ versus T plots were obtained from the peak positions of $d(\chi_M T)/dT$ versus T plots; hysteresis widths were calculated using the relation $\Delta T = (T_{C\uparrow} - T_{C\downarrow})$, as shown in figure 1, thus for each of complexes **1a-c**, at least two different ΔT values are reported. The temperature at which a 1:1 ratio of HS- and LS-states observed is reported as $T_{1/2}$ (Figure 1b).

Complexes **1a** and **1b** showed comparable bistable SCO, as shown in figures 1a and S4, respectively; the SCO remained stable to cycling except for small differences among the cycles. A notable difference is the occurrence of the HS to LS switching at higher temperatures in the second and subsequent cooling steps relative to the first cooling step. Unlike the HS to LS switching, which proceeded in a single step, the LS to HS switching of the complexes proceeded in a stepwise manner. A small plateau-like intermediate region centred around 241 K, featuring almost equal proportions of HS and LS complexes, was observed for **1a** in the LS to HS switching branch of the first cycle. For complex **1b**, such a plateau-like region, centred around 253 K, appeared in the first cycle after reaching a composition in which the HS population (82%) is dominant (Figure S4a). For both the complexes, the onset temperature of plateau-region formation and HS fraction increased with increasing cycle number—the effect is more pronounced for **1a** than **1b**. The occurrence of plateau-like features in the first and subsequent heating cycles resulted in the formation of differently sized hysteresis widths for the complexes. In cycle four, ΔT values of 15 K and 4 K were estimated for **1a** above and below, respectively, the step-like feature (Figure 1b). Similar values were observed for complex **1b** in the fifth cycle (Figure S4b). A $T_{1/2} = \sim 241$ K at $\chi_M T = \sim 1.95 \text{ cm}^3 \text{ mol}^{-1} \text{ K}$ was estimated for **1a** and **1b** in the cycles four and five, respectively.

A lattice solvent-dependent SCO is observed for complex **1c**. In all cycles, the spin-state switching took place in an abrupt manner until a particular LS:HS composition is reached, as shown in figure S5. After that, the switching became gradual, resulting in the formation of two different hysteretic regions composed of dominant HS or LS fractions; for example, such regions featuring $\Delta T = 66$ K and 6 K were observed in the second cycle (Figure S5b). Remarkably, a plateau-like region bridged the abrupt and gradual regions of the first cycle and the LS to HS switching (heating) branch of the second cycle. In the HS to LS switching branch of the second and subsequent cycles, such plateau-like regions disappeared, and the SCO became steadily gradual after the occurrence of initial abrupt switching. The $T_{1/2}$ steadily decreased at each cycle, starting from the first cycle. A $T_{1/2} = 247$ K was obtained for the fourth heating branch, which is close to the value of $T_{1/2} = 243$ K obtained for the heating branches of complexes **1a** (cycle 4) and **1b** (cycle 5). The comparable nature of small- and wide-angle X-ray scattering (SWAXS) patterns (Figure S6) of **1c**—obtained after thermal cycling—and solvent-free **1a** indicates the evolution of the ACN solvated **1c** into a solvent-free phase **1c**, which has a similar molecular organization as well as SCO characteristic—in the fourth heating branch—as that of **1a**. Our attempts to obtain the X-ray structure of solvent-free **1c** was not successful due to the cracking of the crystals during temperature cycling.

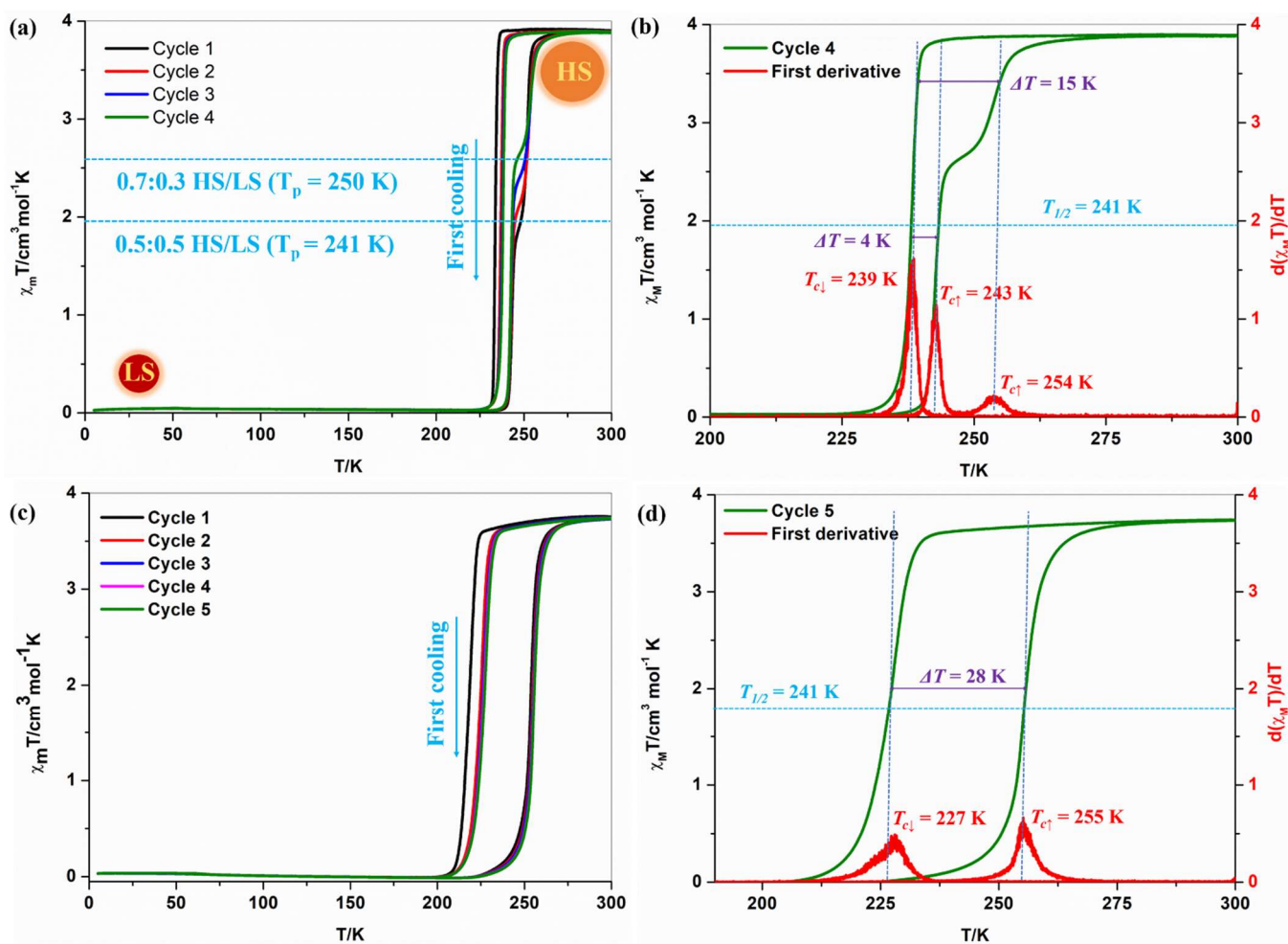


Figure 1. Bistable SCO characteristics of complexes 1a and 2. $\chi_M T$ versus T plots of complex **1a** (a) and **2** (c). $\chi_M T$ versus T and $d(\chi_M T)/dT$ versus T plots of **1a** (b) and **2** (d), corresponding to cycles 4 and 5, respectively. T_p is the temperature at which the centre of the step-like region is situated. The critical temperatures (T_c) associated with the cooling and heating branches are designated as $T_{c\downarrow}$ and $T_{c\uparrow}$, respectively. Experiments were performed in settle mode under an applied DC field of 0.1 T; a scan rate of 5 K/min and 1 K/min were employed for cycles 1-3 and subsequent cycles, respectively.

The rapidly precipitated complex **1d** showed an incomplete and hysteretic SCO with the switching temperature centred around 231 K and 233 K for the first and subsequent cycles, respectively (Figure S7). At 300 K, a $\chi_M T$ value of $2.5 \text{ cm}^3 \text{ mol}^{-1} \text{ K}$ was obtained, indicative of a composition made of a dominant HS fraction contaminated with a LS fraction. As in the cases of **1a** and **1b**, the HS to LS switching of the second and subsequent cycles of **1d** occurred at a higher temperature relative to the first cycle. This resulted in the reduction of thermal hysteresis width associated with cycles 2-5 ($\Delta T = 8 \text{ K}$) in comparison with the first cycle ($\Delta T = 11 \text{ K}$).

Complex **2**— $[\text{Fe}(\text{L})_2](\text{ClO}_4)_2$ —showed bistable SCO with the widest and stable ΔT among the complexes reported in this study; the spin-state switching occurred in a straightforward manner without any intermediate region. In the first cycle, upon cooling from 300 K ($\chi_M T = 3.7 \text{ cm}^3 \text{ mol}^{-1} \text{ K}$), an abrupt HS to LS switching occurred; subsequent heating resulted in the occurrence of LS to HS switching at a higher temperature relative to the HS to LS switching, rendering the SCO hysteretic—a $\Delta T = 35 \text{ K}$ is observed at $T_{1/2} = 237 \text{ K}$. In the second and subsequent cooling, the abrupt HS to LS switching proceeded at a higher temperature relative to the first HS to LS switching. This resulted in the reduction of thermal hysteresis width and an increase of $T_{1/2}$ for the cycles 2-5 relative to the first cycle— $\Delta T = 28 \text{ K}$ and $T_{1/2} = 241 \text{ K}$ were calculated for the fifth cycle.

Differential scanning calorimetry (DSC) experiments further substantiated the reproducible nature of the SCO in complexes **1a**, **1c-d**, and **2**. Since the complexes **1a** and **1b** feature similar SCO characteristics, DSC experiments were not performed for complex **1b**. Overall, the $T_{1/2}$ and ΔT values obtained from the DSC measurements, performed at a scan rate of 2 K/min (Figures 2 and S8), are comparable with the values obtained from magnetic measurements (Table 1).

Table 1. Parameters associated with the SCO of the complexes discussed in this study

Complex	SQUID		DSC	
	$\chi_M T / \text{cm}^3 \text{mol}^{-1} \text{K}$ (at 300 K) ^a	$T_{1/2} / \text{K}$ and $\Delta T / \text{K}$ (at $T_{1/2}$) ^b	$T_{1/2} / \text{K}$ and $\Delta T / \text{K}$ ^{c,d,e}	ΔH and ΔS ^{f,g}
1a	3.87	241 and 4 (cycle 4)	240 and 6 (Cycle 4)	13.8 and 57.5
1b	3.91	241 and 4 (cycle 5)		
1c	3.11	276 and 36 (cycle 1)		
1d	2.47	233 and 7 (cycle 5)	234 and 8	8.15 and 34.83
2	3.75	247 and 28 (cycle 5)	241 and 32 (Cycle 4)	12.36 and 51.29

^aFor the last performed cycle; ^bScan rate = 1 K/min; ^cScan rate = 2 K/min; ^dDSC measurements were not performed for **1b**; ^ethe thermodynamic parameters were not calculated for **1c** due to the unstable nature of the SCO; ^fcalculated using the relation $\Delta S = \Delta H / T_{1/2}$; ^g ΔH in kJ mol⁻¹ and ΔS in J K⁻¹ mol⁻¹.

The DSC experiments were also used to derive the enthalpy (ΔH) and entropy (ΔS) variations associated with the SCO of the complexes. Although valid only for the case of solution-phase SCO, the relation $\Delta S = \Delta H / T_{1/2}$ is often used in the literature to describe the entropy variation associated with spin-state switching in the solid-state.⁴³ Therefore, to facilitate a meaningful comparison with the literature reported values, we have used the relation $\Delta S = \Delta H / T_{1/2}$ to calculate the entropy values associated with the SCO of the complexes. The experimentally deduced ΔH and ΔS values collected in table 1 are in the range reported for iron(II)-SCO complexes.^{43,44} As often reported, the entropy values are greater than 13.4 J K⁻¹ mol⁻¹ expected solely on the S = 0 to S = 2 spin multiplicity change occurring upon SCO: the excess entropy is ascribed to the differing intramolecular vibrational modes coupled with the spin-state switching of the complexes.^{45,46}

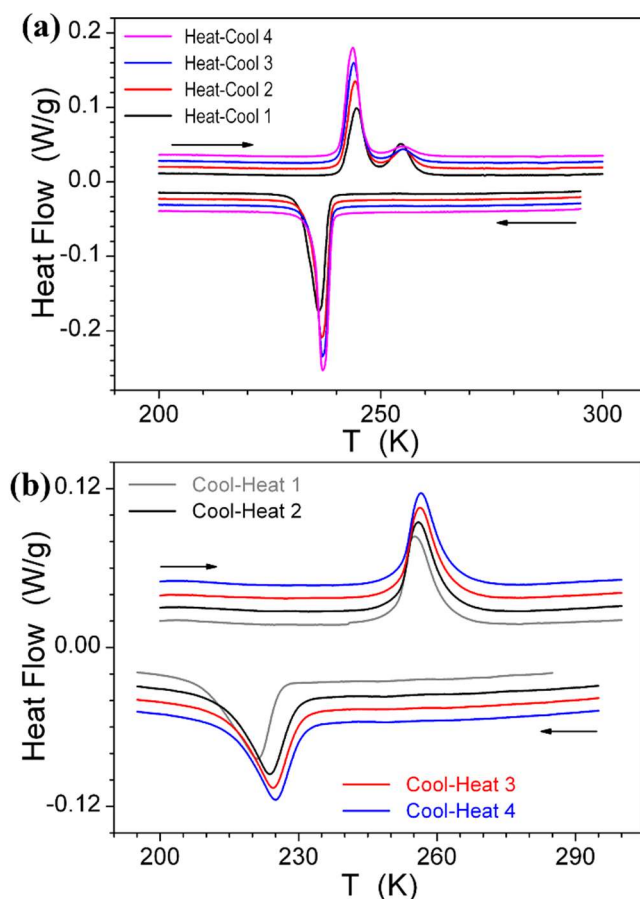


Figure 2. Differential scanning calorimetry (DSC) curves of complexes (a) **1a** and (b) **2**. A scanning rate of 2 K/min was employed; endotherm (up). The close correlation between the $\chi_m T$ versus T plots (Figure 1) and DSC curves confirms the reproducible nature of the SCO associated with the complexes discussed in this study.

The complexes reported in this study are remarkable because they show abrupt and hysteretic spin-state switching. In the absence of single-crystal X-ray diffraction studies, it is difficult to ascribe the factors contributing to the occurrence of hysteretic SCO behaviour in complexes **1a-b**, **1d**, and **2**. However, some tentative insights could be drawn from the literature reports describing SCO in $[\text{Fe}(\text{BPP-R})_2]^{2+}$ series of complexes. Although the spin-state switching in $[\text{Fe}(\text{BPP-R})_2]^{2+}$ complexes is often reported to proceed with thermal hysteresis widths in the range of 1-4 K, only a handful of $[\text{Fe}(\text{BPP-R})_2]^{2+}$ complexes are reported to show SCO with ΔT larger than 4 K. Notable examples are $[\text{Fe}(\text{BPP-COOEt})_2](\text{ClO}_4)_2 \cdot 1\text{CH}_3\text{CN}$,⁴⁰ $[\text{Fe}(\text{BPP-CH}_2\text{Br})_2](\text{BF}_4)_2 \cdot 4\text{MeNO}_2$,⁴⁷ and $[\text{Fe}(\text{BPP-CH}_3)_2](\text{ClO}_4)_2$.⁴³ Complex $[\text{Fe}(\text{BPP-COOEt})_2](\text{ClO}_4)_2 \cdot 1\text{CH}_3\text{CN}$ showed abrupt and hysteretic SCO with $\Delta T = \sim 101$ K ($T_{1/2} = 233$ K); however, the SCO of the complex is not stable and varied with cycling. Thermal hysteresis widths of 31 K ($T_{1/2} = 340$ K) and 18 K ($T_{1/2} = 184$ K) were reported for $[\text{Fe}(\text{BPP-CH}_2\text{Br})_2](\text{BF}_4)_2 \cdot 4\text{MeNO}_2$ and $[\text{Fe}(\text{BPP-CH}_3)_2](\text{ClO}_4)_2$, respectively. While the SCO profile of $[\text{Fe}(\text{BPP-CH}_3)_2](\text{ClO}_4)_2$ is comparable,

except for $T_{1/2}$ and ΔT , with the one observed for complex **2**, the SCO in $[\text{Fe}(\text{BPP-CH}_2\text{Br})_2](\text{BF}_4)_2 \cdot 4\text{MeNO}_2$ is gradual. Thus, the 28 K thermal hysteresis width reported in this study for complex **2** is the widest stable ΔT so far reported for a $[\text{Fe}(\text{BPP-R})_2]^{2+}$ complex, exhibiting abrupt spin-state switching.

Attempts have been made to establish the relation between bistable SCO and molecular organization in the iron(II)-BPP family of complexes. Thereby, a terpyridine embrace packing pattern⁴² and Jahn-teller (J-T) distorted HS-states have been attributed to the occurrence of hysteretic SCO in $[\text{Fe}(\text{BPP-CH}_2\text{Br})_2](\text{BF}_4)_2 \cdot 4\text{MeNO}_2$ and $[\text{Fe}(\text{BPP-CH}_3)_2](\text{ClO}_4)_2$. On the other hand, a J-T distorted HS-state and non-terpyridine embrace packing pattern was observed for $[\text{Fe}(\text{BPP-COOEt})_2](\text{ClO}_4)_2 \cdot 1\text{CH}_3\text{CN}$, which showed $\Delta T = 101$ K. The bistable SCO in complex $[\text{Fe}(\text{BPP-COOEt})_2](\text{ClO}_4)_2 \cdot 1\text{CH}_3\text{CN}$ is thus primarily ascribed to the occurrence of a pronounced J-T distortion in combination with some favourable intermolecular interactions.⁴⁰ Specifically, while the elastic intermolecular interactions propagate the spin-state switching information throughout the lattice, the J-T distortion would act as a barrier and energetically separate the HS- and LS states of complex $[\text{Fe}(\text{BPP-COOEt})_2](\text{ClO}_4)_2 \cdot 1\text{CH}_3\text{CN}$, causing the formation of ~ 101 K wide hysteresis loop. Based on the above discussion, we assume J-T distorted nature of the HS-states of **1a-d** and **2**, effecting hysteretic spin-state switching in the complexes. The abruptness of the transition observed for **1a-b** and **2** could have arisen due to favourable intermolecular contacts propagating the spin-state switching throughout the crystal lattice. As a note to the reader, the above reductionist approach, attempting to rationalize SCO in complexes **1a-d** and **2** needs to be considered with caution; other structural factors such as anion disorder, electrostatics, etc., could have also contributed to the hysteretic SCO in the complexes.¹³

The situation is rather complicated for complex **1c**, which showed lattice solvent-dependent SCO upon repeated heat-cool cycling. Such SCO is commonly observed for complexes crystallizing with lattice solvent molecules. And indeed, the high sensitivity of the SCO to the presence or absence of lattice solvent molecules is a well-established phenomenon in the SCO research field. On the other hand, stepwise SCO is not a common occurrence in the case of mononuclear complexes such as $[\text{Fe}(\text{BPP-R})_2]^{2+}$ complexes; only a handful $[\text{Fe}(\text{BPP-R})_2]^{2+}$ complexes have been reported showing stepwise SCO behaviour. It is interesting to note the step-like features present in the LS to HS switching branches of **1c**. Although less pronounced, such step-like features also appeared in the LS to HS branches of **1a-b**. In all cases, the SCO became more gradual after reaching stepwise features, effecting the formation of larger hysteresis widths relative to the ones observed for the abrupt SCO regions, which appeared below the onset of step-like features. Such observations point to the formation of a phase composed of specific proportions of LS and HS states—for example, 1:1 HS/LS observed at 241 K for **1a**. The nature of intermolecular interactions varies in the low- and high-temperature phases, causing the observed abrupt versus gradual SCO behaviour. The absence of

such stepwise LS to HS switching in deliberately precipitated **1d** indicates the requirement of high-quality crystals with a singular arrangement, inducing step-like SCO features. Besides, the more broadened reflections observed in the SWAXS patterns of **1d** relative to **1a** indicate different crystal sizes of the complexes with the size of **1d** in the nanometre range. Overall, the observed difference in the SCO between **1a** and **1d** could be attributed either to a specific crystalline arrangement or to the different sizes of the crystals. It is also possible that both the factors contribute to the observed difference; an unambiguous elucidation requires further experimental investigations.

In conclusion, the pursuit of SCO complexes featuring technologically relevant thermal hysteresis width ($\Delta T \geq 40$ K) centred at or around room temperature is still on. However, the bistable SCO characteristics associated with the complexes reported in this study is encouraging to pursue $[\text{Fe}(\text{BPP-R})_2]^{2+}$ family of complexes for the realization of technologically relevant SCO systems. The amenable nature of -CN group for further functional group transformation is ideally suited to design bistable $[\text{Fe}(\text{BPP-R})_2]^{2+}$ SCO complexes. For example, the conversion of the -CN group to the tetrazole functional group could be used to construct an SCO-active lattice composed of hydrogen bond-forming self-assembling motifs. Moreover, deprotonation of the same tetrazole tethered BPP-ligand system under basic conditions could yield a monoanionic ligand useful for the preparation of charge-neutral SCO complexes—such complexes are reported to undergo bistable SCO at or around room temperature.^{48,49}

Conflicts of interest

There are no conflicts of interest to declare.

Acknowledgements

The authors thank Dr. Guillaume Rogez, IPCMS, for the SQUID measurements. Grant Agency Innovation FRC is acknowledged for the financial support for the project Self-assembly of spin-crossover (SCO) complexes on graphene. M.R. thanks the DFG priority program 1928 “COORNETS” for generous support.

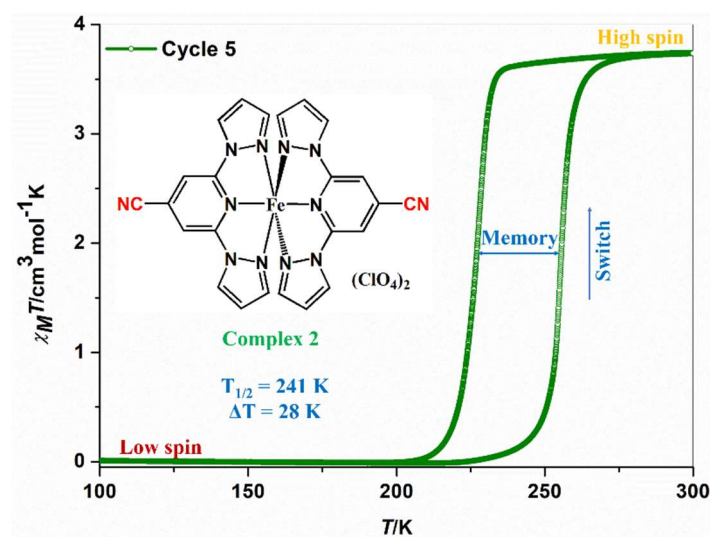
References

- 1 P. Gülich and H. A. Goodwin, Eds., *Spin Crossover in Transition Metal Compounds I*, Springer Berlin, Heidelberg, 2004, vol. 233.
- 2 M. A. Halcrow, *Spin-crossover Materials: Properties and Applications*, Wiley, 2013.
- 3 K. Ridier, Y. Zhang, M. Piedrahita-Bello, C. M. Quintero, L. Salmon, G. Molnár, C. Bergaud and A. Bousseksou, *Adv. Mater.*, 2020, 2000987.
- 4 M. Palluel, N. M. Tran, N. Daro, S. Buffière, S. Mornet, E. Freysz and G. Chastanet, *Adv. Funct. Mater.*, 2020, **30**, 2000447.
- 5 E. P. Geest, K. Shakouri, W. Fu, V. Robert, V. Tudor, S. Bonnet and G. F. Schneider, *Adv. Mater.*, 2020, **32**, 1903575.

- 6 G. Molnár, M. Mikolasek, K. Ridier, A. Fahs, W. Nicolazzi and A. Bousseksou, *Ann. Phys.*, 2019, **531**, 1900076.
- 7 H.-Y. Sun, Y.-S. Meng and T. Liu, *Chem. Commun.*, 2019, **55**, 8359–8373.
- 8 S. Decurtins, P. Güthlich, C. P. Köhler, H. Spiering and A. Hauser, *Chem. Phys. Lett.*, 1984, **105**, 1–4.
- 9 A. Hauser, *Comments Inorg. Chem.*, 1995, **17**, 17–40.
- 10 J.-F. Létard, P. Guionneau and L. Goux-Capes, in *Spin Crossover in Transition Metal Compounds III*, Springer-Verlag, Berlin/Heidelberg, 2004, vol. 235, pp. 221–249.
- 11 A. Bousseksou, G. Molnár, L. Salmon and W. Nicolazzi, *Chem. Soc. Rev.*, 2011, **40**, 3313.
- 12 E. Collet and P. Guionneau, *Comptes Rendus Chim.*, 2018, **21**, 1133–1151.
- 13 M. A. Halcrow, *Chem. Soc. Rev.*, 2011, **40**, 4119.
- 14 G. J. Halder, *Science*, 2002, **298**, 1762–1765.
- 15 R. W. Hogue, S. Singh and S. Brooker, *Chem. Soc. Rev.*, 2018, **47**, 7303–7338.
- 16 O. Kahn, *Curr. Opin. Solid State Mater. Sci.*, 1996, **1**, 547–554.
- 17 M. Ruben, J. Rojo, F. J. Romero-Salguero, L. H. Uppadine and J.-M. Lehn, *Angew. Chem. Int. Ed.*, 2004, **43**, 3644–3662.
- 18 J. Tao, R.-J. Wei, R.-B. Huang and L.-S. Zheng, *Chem Soc Rev*, 2012, **41**, 703–737.
- 19 P. Guionneau, *Dalton Trans*, 2014, **43**, 382–393.
- 20 S. Venkataramani, U. Jana, M. Dommaschk, F. D. Sonnichsen, F. Tuzek and R. Herges, *Science*, 2011, **331**, 445–448.
- 21 M. A. Halcrow, *Chem. Lett.*, 2014, **43**, 1178–1188.
- 22 O. Kahn, J. Kröber and C. Jay, *Adv. Mater.*, 1992, **4**, 718–728.
- 23 M. Ruben and K. S. Kumar, *Angew. Chem. Int. Ed.*, , DOI:10.1002/anie.201911256.
- 24 K. Senthil Kumar and M. Ruben, *Coord. Chem. Rev.*, 2017, **346**, 176–205.
- 25 A. Köbke, F. Gutzeit, F. Röhricht, A. Schlimm, J. Grunwald, F. Tuzek, M. Studniarek, D. Longo, F. Choueikani, E. Otero, P. Ohresser, S. Rohlf, S. Johannsen, F. Diekmann, K. Rossnagel, A. Weismann, T. Jasper-Toennies, C. Näther, R. Herges, R. Berndt and M. Gruber, *Nat. Nanotechnol.*, 2020, **15**, 18–21.
- 26 K. P. Kepp, *Coord. Chem. Rev.*, 2017, **344**, 363–374.
- 27 Z. Wu, *J. Geophys. Res. Solid Earth*, 2016, **121**, 2304–2314.
- 28 T. Miyamachi, M. Gruber, V. Davesne, M. Bowen, S. Boukari, L. Joly, F. Scheurer, G. Rogez, T. K. Yamada, P. Ohresser, E. Beaurepaire and W. Wulfhekel, *Nat. Commun.*, , DOI:10.1038/ncomms1940.
- 29 B. Weber, W. Bauer and J. Obel, *Angew. Chem. Int. Ed.*, 2008, **47**, 10098–10101.
- 30 B. Schäfer, C. Rajnák, I. Šalitroš, O. Fuhr, D. Klar, C. Schmitz-Antoniak, E. Weschke, H. Wende and M. Ruben, *Chem. Commun.*, 2013, **49**, 10986.
- 31 H. Hagiwara, T. Masuda, T. Ohno, M. Suzuki, T. Udagawa and K. Murai, *Cryst. Growth Des.*, 2017, **17**, 6006–6019.
- 32 C. Lochenie, K. Schötz, F. Panzer, H. Kurz, B. Maier, F. Puchtler, S. Agarwal, A. Köhler and B. Weber, *J. Am. Chem. Soc.*, 2018, **140**, 700–709.
- 33 J. M. Holland, C. A. Kilner, M. Thornton-Pett, M. A. Halcrow, J. A. McAllister and Z. Lu, *Chem. Commun.*, 2001, 577–578.
- 34 L. J. Kershaw Cook, R. Kulmaczewski, R. Mohammed, S. Dudley, S. A. Barrett, M. A. Little, R. J. Deeth and M. A. Halcrow, *Angew. Chem. Int. Ed.*, 2016, **55**, 4327–4331.
- 35 L. J. Kershaw Cook, R. Mohammed, G. Sherborne, T. D. Roberts, S. Alvarez and M. A. Halcrow, *Coord. Chem. Rev.*, 2015, **289–290**, 2–12.
- 36 M. A. Halcrow, *New J Chem*, 2014, **38**, 1868–1882.
- 37 M. A. Halcrow, *Coord. Chem. Rev.*, 2009, **253**, 2493–2514.
- 38 M. A. Halcrow, *Coord. Chem. Rev.*, 2005, **249**, 2880–2908.
- 39 M. Halcrow, *Crystals*, 2016, **6**, 58.

- 40 K. Senthil Kumar, B. Heinrich, S. Vela, E. Moreno-Pineda, C. Bailly and M. Ruben, *Dalton Trans.*, 2019, **48**, 3825–3830.
- 41 In *Comprehensive Organic Name Reactions and Reagents*, John Wiley & Sons, Inc., Hoboken, NJ, USA, 2010.
- 42 R. Pritchard, C. A. Kilner and M. A. Halcrow, *Chem Commun*, 2007, 577–579.
- 43 L. J. Kershaw Cook, F. L. Thorp-Greenwood, T. P. Comyn, O. Cespedes, G. Chastanet and M. A. Halcrow, *Inorg. Chem.*, 2015, **54**, 6319–6330.
- 44 M. Sorai, Y. Nakazawa, M. Nakano and Y. Miyazaki, *Chem. Rev.*, 2013, **113**, PR41–PR122.
- 45 W. Nicolazzi and A. Bousseksou, *Comptes Rendus Chim.*, 2018, **21**, 1060–1074.
- 46 A. Bousseksou, J. J. McGarvey, F. Varret, J. A. Real, J.-P. Tuchagues, A. C. Dennis and M. L. Boillot, *Chem. Phys. Lett.*, 2000, **318**, 409–416.
- 47 H. Douib, L. Cornet, J. F. Gonzalez, E. Trzop, V. Dorcet, A. Gouasmia, L. Ouahab, O. Cador and F. Pointillart, *Eur. J. Inorg. Chem.*, 2018, **2018**, 4452–4457.
- 48 K. Senthil Kumar, S. Vela, B. Heinrich, N. Suryadevara, L. Karmazin, C. Bailly and M. Ruben, *Dalton Trans.*, 2020, **49**, 1022–1031.
- 49 K. Senthil Kumar, I. Šalitroš, B. Heinrich, O. Fuhr and M. Ruben, *J. Mater. Chem. C*, 2015, **3**, 11635–11644.

TOC Graphic



Abrupt and hysteretic (bistable) spin-crossover (SCO) characteristics of $[\text{Fe}(\text{BPP-CN})_2](\text{X})_2$ — $\text{X} = \text{BF}_4$ (**1a-d**) or ClO_4 (**2**)—family of complexes are reported.

Supporting Information

Bistable spin-crossover in a new series of $[\text{Fe}(\text{BPP-R})_2]^{2+}$ (BPP = 2,6-bis(pyrazol-1-yl)pyridine; R = CN) complexes

Kuppusamy Senthil Kumar,^{a,b,*} Nicolas DelGiudice,^a Benoît Heinrich,^a Laurent Douce,^a and Mario Ruben^{a,b,d,*}

^aInstitut de Physique et Chimie des Matériaux de Strasbourg (IPCMS), CNRS-Université de Strasbourg, 23, rue du Loess, BP 43, 67034 Strasbourg cedex 2, France.

^bInstitute of Nanotechnology (INT), Karlsruhe Institute of Technology (KIT), Hermann-von-Helmholtz-Platz 1, 76344, Eggenstein-Leopoldshafen, Germany.

^cService de Radiocristallographie, Fédération de Chimie Le Bel FR2010 CNRS-Université de Strasbourg, 1 rue Blaise Pascal, BP 296/R8, 67008 Strasbourg cedex, France.

^dInstitute of Quantum Materials and Technologies (IQMT), Karlsruhe Institute of Technology (KIT), Hermann-von-Helmholtz-Platz 1, 76344, Eggenstein-Leopoldshafen, Germany.

*e-mail: kavinsenthil82@gmail.com; mario.ruben@kit.edu

Contents

S1. Materials and Instrumentation.....	14
S2. Synthesis and characterization of the ligand (L) and complexes 1a-d and 2	15
S3. Crystal structure analysis of 1c	16
S4. UV-vis spectra of the ligand and complexes 1a and 2	18
S5. Spin-crossover characteristics of complexes 1b-d and Small- and wide-angle X-ray scattering studies of complexes 1a , 1c , and 1d	19
S6. Differential scanning calorimetry studies of complexes 1c and 1d	22

Experimental

S1. Materials and Instrumentation

Materials

Anhydrous solvents, CuCN, Fe(BF₄)₂·6H₂O, and Fe(ClO₄)₂·6H₂O were purchased from commercial sources and used as received. Glassware were dried in a vacuum oven at 150°C prior to the experiments. Chemical reactions reported in this study were performed under argon (Ar) atmosphere.

Instrumentation

X-ray crystallography

X-Ray diffraction data collection was carried out on a Bruker APEX II DUO Kappa-CCD diffractometer equipped with an Oxford Cryosystem liquid N₂ device, using Cu-K α radiation ($\lambda = 1.54178$ Å). The crystal-detector distance was 40 mm. The cell parameters were determined (APEX2 software) [1] from reflections taken from three sets of 20 frames, each at 10s exposure. The structure was solved by Direct methods using the program SHELXS-2014 [2]. The refinement and all further calculations were carried out using SHELXL-2014 [2]. The H-atoms were included in calculated positions and treated as riding atoms using SHELXL default parameters. The non-H atoms were refined anisotropically, using weighted full-matrix least-squares on F². A semi-empirical absorption correction was applied using SADABS in APEX2 [1]; transmission factors: T_{min}/T_{max} = 0.5220/0.7528.

UV-Vis absorption spectral measurements

Absorption spectra were measured on Varian Cary 100 double-beam UV–VIS spectrophotometer and baseline corrected.

Magnetic measurements

All the reported magnetic measurements were performed on a MPMS-XL5 SQUID magnetometer (Quantum Design). For the standard magnetic measurement in the dark, the temperature dependent magnetization was recorded at an applied DC field of 0.1 T. Temperature sweeping rates of 3 K min⁻¹ and 1 K min⁻¹ were employed. Gelatine capsules were used as sample holders in the temperature range 5 \leftrightarrow 385 K. The diamagnetic corrections of the molar magnetic susceptibilities were applied using Pascal's constants.

Differential scanning calorimetry (DSC) and small- and wide-angle X-ray scattering (SWAXS) measurements

DSC measurements were performed with a TA Instruments DSCQ1000 instrument operated at a scanning rate of 2 K min⁻¹ on heating and on cooling. SWAXS patterns were obtained with a linear monochromatic Cu K α 1 beam (λ = 1.5405 Å) obtained using a sealed-tube generator equipped with a bent quartz monochromator and a curved Inel CPS 120 counter gas filled detector; periodicities up to 70 Å can be measured, and the sample temperature controlled to within ± 0.01 °C from 20 to 200 °C. The sample was filled in Lindemann capillaries and exposure times were varied between 1 and 24 hours.

S2. Synthesis and characterization of the ligand (L) and complexes 1a-d and 2

Synthesis of 2,6-di(1H-pyrazol-1-yl)pyridine-4-carbonitrile (L): Copper(I)cyanide (0.323 g, 3.6×10^{-3} M) was added to a solution of 4-iodo-2,6-di(1H-pyrazol-1-yl)pyridine (1 g, $\sim 3 \times 10^{-3}$ M) in 5 ml of dry DMF, and the reaction mixture was stirred at 130°C for 12 h under argon protection. One gram of KCN dissolved in 10 mL of water was added to the cooled reaction mixture, and the mixture was stirred for 30 min and filtered. The filtrate was diluted with more water and extracted with DCM three times. The combined organic fractions were stored over Na₂SO₄ for 2 h. Column chromatography with silica gel and DCM as stationary and mobile phases, respectively, yielded the ligand as white powder.

Yield: 0.5 g (71%)

¹H NMR (CDCl₃, 500 MHz): 8.56 (dd, J = 2.68 and 0.65), 8.10 (s), 7.84 (dd, J = 1.59 and 0.61) and 6.58 (dd, J = 2.66 and 1.64). **¹³C NMR (CDCl₃, 125 MHz):** 150.8, 143.5, 127.3, 125.2, 115.9, 111.2, 109.1. **ESI-MS:** Calculated for C₁₂H₉N₆ [M+H]⁺ = 237.09; found 237.09. **Elemental analysis:** Calculated for C₁₂H₈N₆: C 61.01 H 3.41 N 35.58; found C 60.75 H 3.41 N 35.40.

Preparation of complexes 1a-c: To one eq. of ligand dissolved in 10 mL of *dry acetonitrile*, Fe(BF₄)₂·6H₂O (0.5 eq.) was added as a solid, and the mixture was swirled for a few seconds or until the occurrence of solubilization of the iron(II) salt. The reaction mixture was allowed to stand for a week, leading to the deposition of orange plate-like solids (**1a**), which were filtered off, washed with ether, and dried under vacuum overnight.

The filtrate was portioned into test tubes and diethyl ether was allowed to slow-diffuse into the test tubes at 4°C. This process resulted in the formation of orange plate-like (**1b**) and red-rod shaped (**1c**·ACN) crystals. The crystals were separated for analyses.

Elemental analysis of 1a: Calculated for C₂₄H₁₆FeN₁₂B₂F₈: C, 41.07; H, 2.30; N, 23.95. Found: C, 41.14, H, 2.32, N, 23.78.

Elemental analysis of 1b: Calculated for C₂₄H₁₆FeN₁₂B₂F₈: C, 41.07; H, 2.30; N, 23.95. Found: C, 41.10, H, 2.34, N, 23.70.

Elemental analysis of 1c: Calculated for $C_{24}H_{16}FeN_{12}B_2F_8 \cdot 1CH_3CN$: C, 42.03; H, 2.58; N, 24.51. Found: C, 41.33, H, 2.42, N, 24.02. The discrepancy between the calculated and obtained values are due to the loss of lattice ACN solvent.

Complex 1d: To one eq. of ligand dissolved in 10 mL of dry acetonitrile and dichloromethane (1:1 v/v) solvent mixture, $Fe(BF_4)_2 \cdot 6H_2O$ (0.5 eq) was added as a solid, and the mixture was stirred for two hours, leading to the formation of a precipitate. The precipitate was filtered, washed with dichloromethane twice, and dried under vacuum to yield an orange-red powder (**1d**).

Elemental analysis: Calculated for $C_{24}H_{16}FeN_{12}B_2F_8$: C, 41.07; H, 2.30; N, 23.95. Found: C, 40.60, H, 2.32, N, 23.43.

Complex 2: To one eq. of ligand dissolved in 10 mL of dry acetonitrile, $Fe(ClO_4)_2 \cdot 6H_2O$ (0.5 eq.) was added as a solid, an immediate precipitation occurred. The mixture was stirred for two hours, filtered, and the precipitate was washed with ether twice. Drying of the solids under vacuum yielded an orange powder (**2**).

Elemental analysis: Calculated for $C_{24}H_{16}FeN_{12}Cl_2O_8$: C, 39.64; H, 2.22; N, 23.11. Found: C, 39.43; H, 2.27; N, 22.62.

S3. Crystal structure analysis of 1c

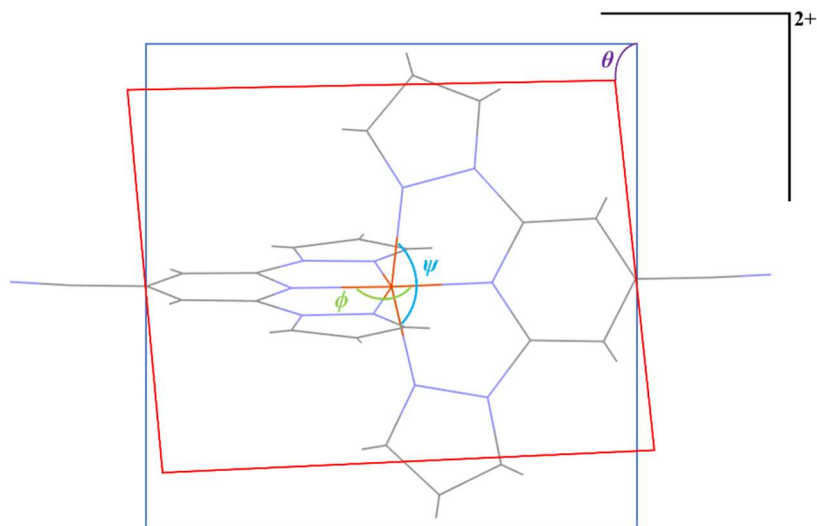


Chart S1. Structural model depicting angular components in $[Fe(1-BPP-CN)_2](BF_4)_2 \cdot CH_3CN$ (**1c**). The angles ϕ and θ represent the degree of distortion; complexes with ideal octahedral geometry have $\phi = 180^\circ$ and $\theta = 90^\circ$. The N{pyrazole}-Fe-N{pyrazole} clamp angle is represented as ψ . See the table below for actual values.

Table S1. Selected bond lengths (Å), angles, and distortion indices (°) of complex **1c**. α is the average value of four cis-N{pyridyl}-Fe- N{pyrazole} angles; Σ is the distortion index, calculated using the relation $\Sigma_{i=1}^{i=12} = |90 - i|$, where i is one of the twelve cis-N-Fe-N angles.

Parameter	Value	Parameter	Value
T/K	293	rFe-N(Average)	1.9(4)
rFe ₁ -N ₁ (pyrazolyl)	1.976(7)	N ₃ -Fe ₁ -N ₉ (ϕ)	176.9(3)
rFe ₁ -N ₃ (pyridyl)	1.891(5)	N7-Fe ₁ -N ₁₂ (ψ)	160.4(3)
rFe ₁ -N ₄ (pyrazolyl)	1.958(7)	N ₁ -Fe ₁ -N ₄ (ψ)	161.1(3)
rFe ₁ -N ₇ (pyrazolyl)	1.973(6)	Σ	84.0(6)
rFe ₁ -N ₉ (pyridyl)	1.885(5)	θ	85.4(4)
Fe ₁ -N ₁₂ (pyrazolyl)	1.964(6)	α	80.4(0)

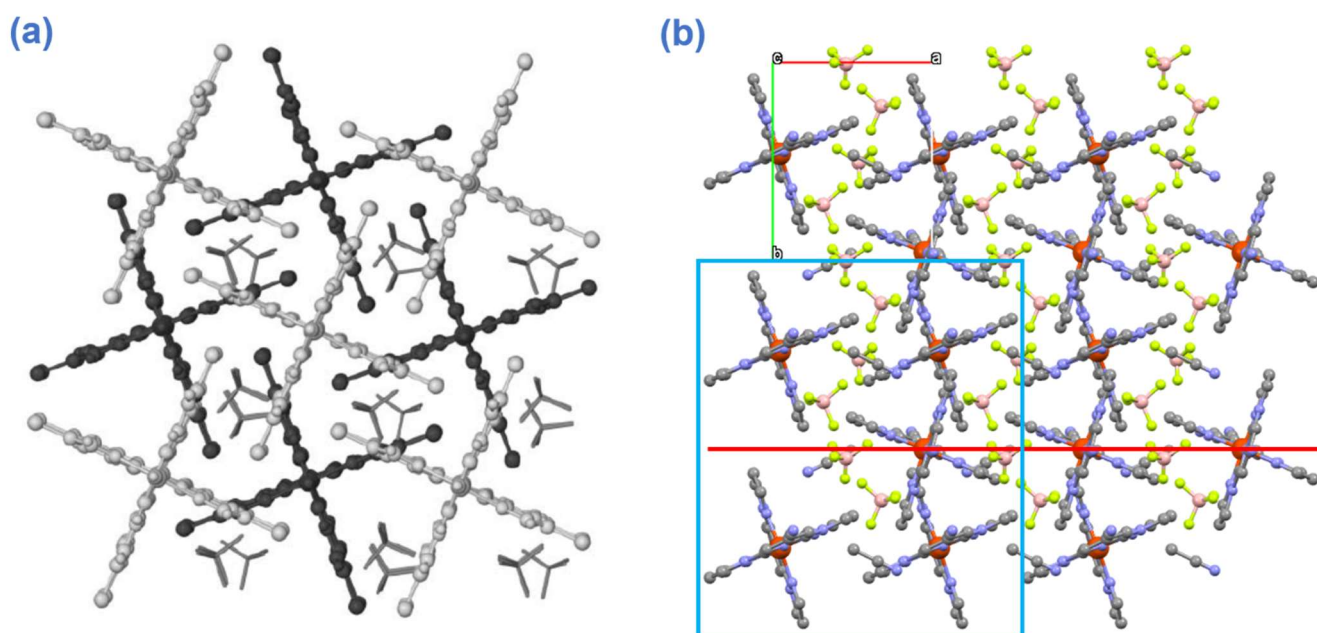


Figure S1. Typical terpyridine embrace lattice packing pattern observed in an $[\text{Fe}(\text{1-BPP-R})_2](\text{X})_2$ family of complexes (Image reproduced from reference 3; copyright Royal Society of Chemistry). (b) Molecular packing in complex **1c** followed a non-terpyridine embrace lattice packing pattern.

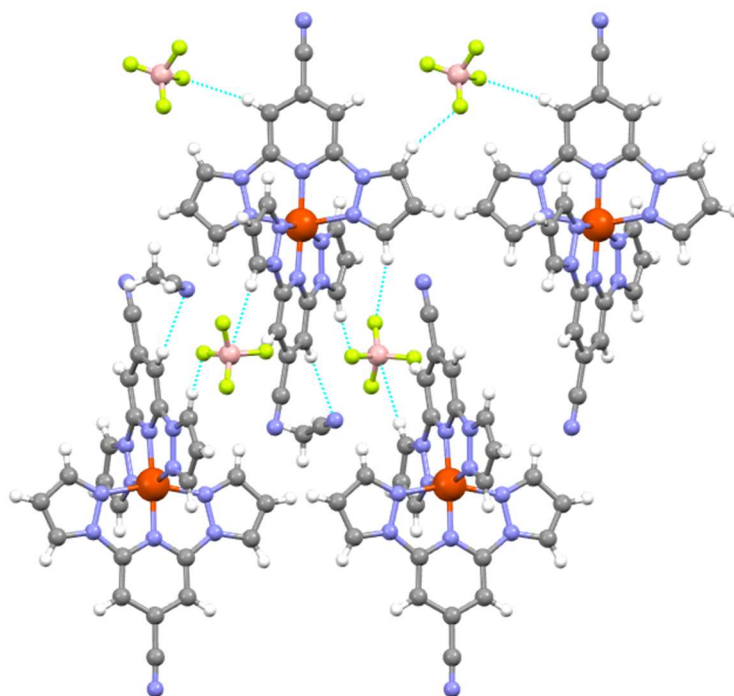


Figure S2. Intermolecular short contacts observed in the crystal lattice of **1c**.

S4. UV-vis spectra of the ligand and complexes **1a** and **2**

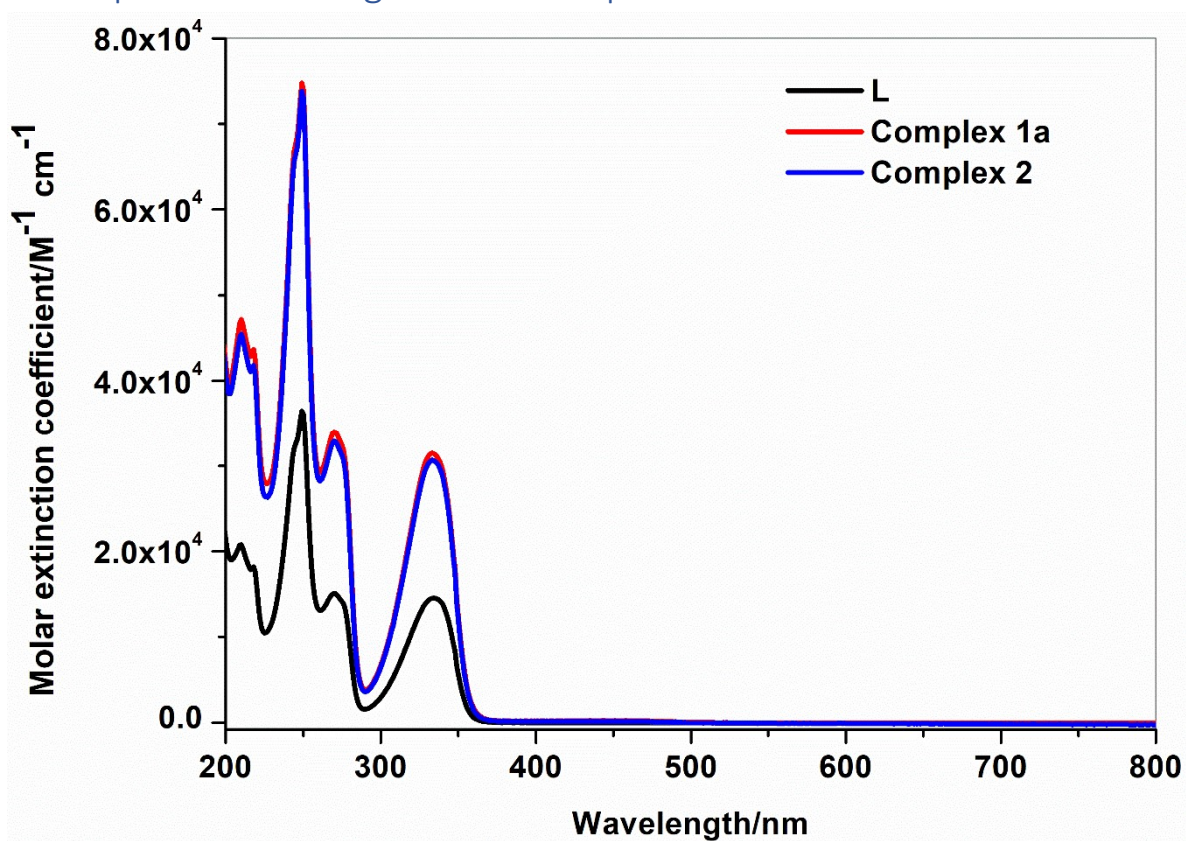


Figure S3. UV-vis absorption spectra of the ligand and complexes **1a** and **2**. Spectrophotometric grade ACN was used as a solvent.

Table S2. Absorption maxima and molar extinction coefficients of the ligands and complexes

Entry	$\lambda_{\text{max,abs}} (\epsilon)$ [nm, ($10^4 \text{ M}^{-1} \text{ cm}^{-1}$)]
L	210 (2.06), 218 (1.82), 245 (3.21), 249 (3.66), 270 (1.48), 276 (1.36), 335 (1.47)
Complex 1a	210 (4.7), 218 (4.34), 244 (6.72), 249 (7.49), 270 (3.41), 276 (3.2), 334 (3.18)
Complex 2	210 (4.54), 218 (4.17), 245 (6.58), 249 (7.36), 270 (3.28), 276 (3.07), 333 (3.06)

S5. Spin-crossover characteristics of complexes **1b-d** and Small- and wide-angle X-ray scattering studies of complexes **1a**, **1c**, and **1d**

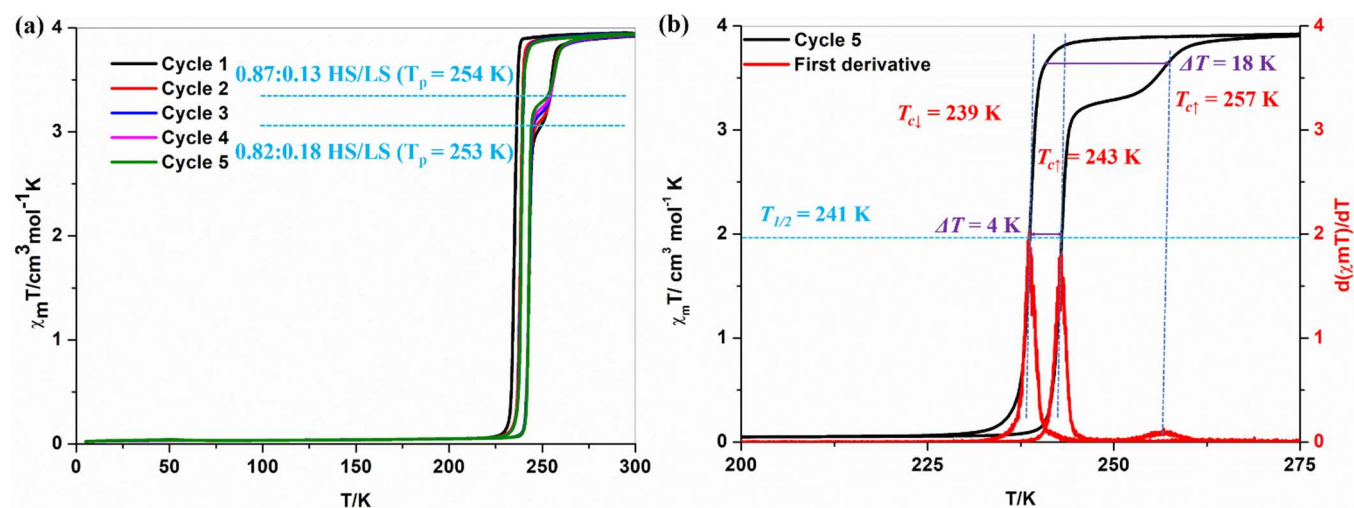


Figure S4. (a) $\chi_M T$ versus T plots of complex **1b**, and (b) $\chi_M T$ versus T and $d(\chi_M T)/dT$ versus T plots of complex **1b**, corresponding to cycle 5. T_p is the temperature, where the centre of the step-like region situated. The critical temperatures (T_c) associated with the cooling and heating branches are designated as $T_{c\downarrow}$ and $T_{c\uparrow}$, respectively.

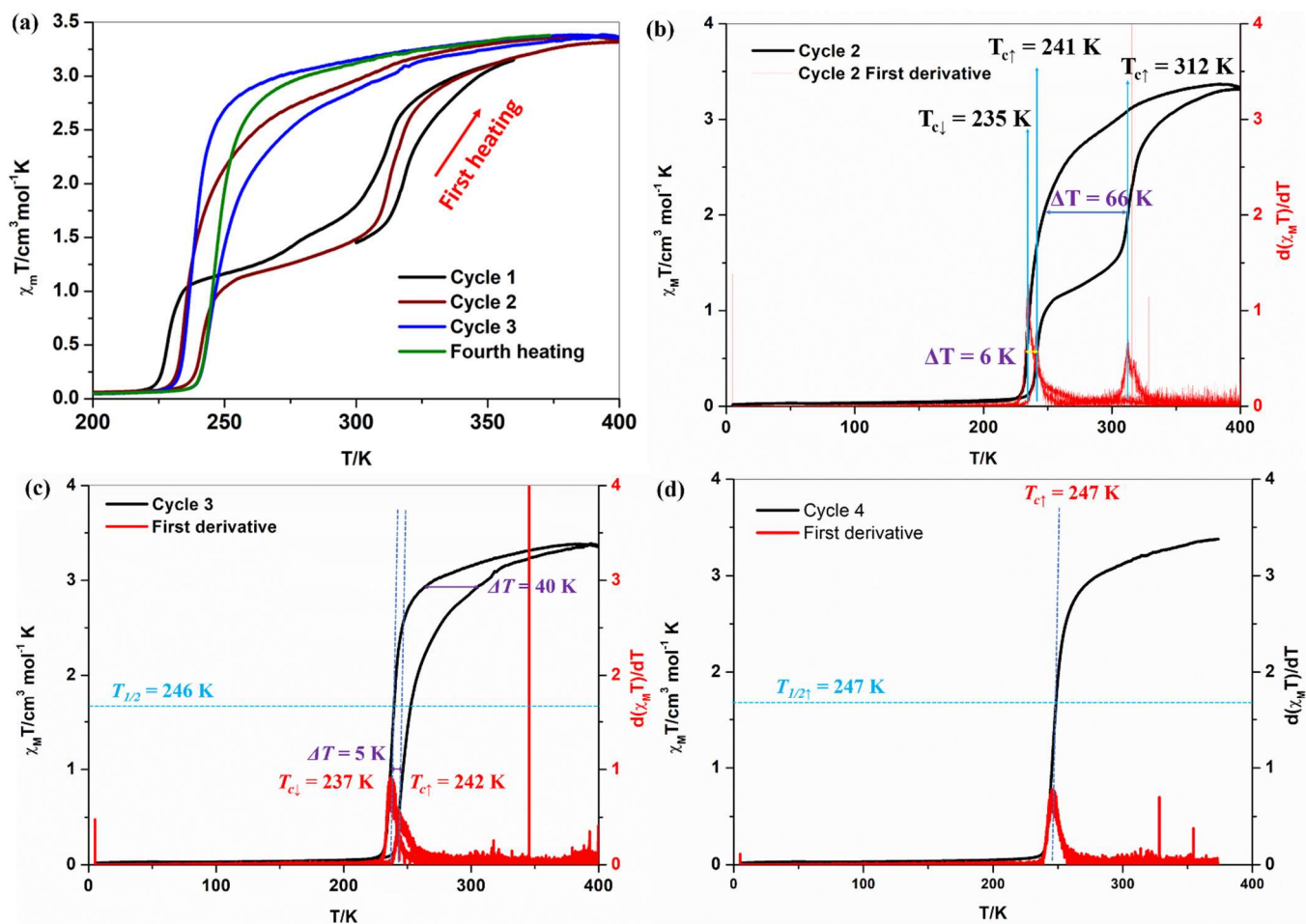


Figure S5. (a) $\chi_M T$ versus T plots and (b-c) $d(\chi_M T)/dT$ versus T and $\chi_M T$ versus T plots of complex **1c**. The critical temperatures (T_c) associated with the cooling and heating branches are designated as $T_{c\downarrow}$ and $T_{c\uparrow}$, respectively.

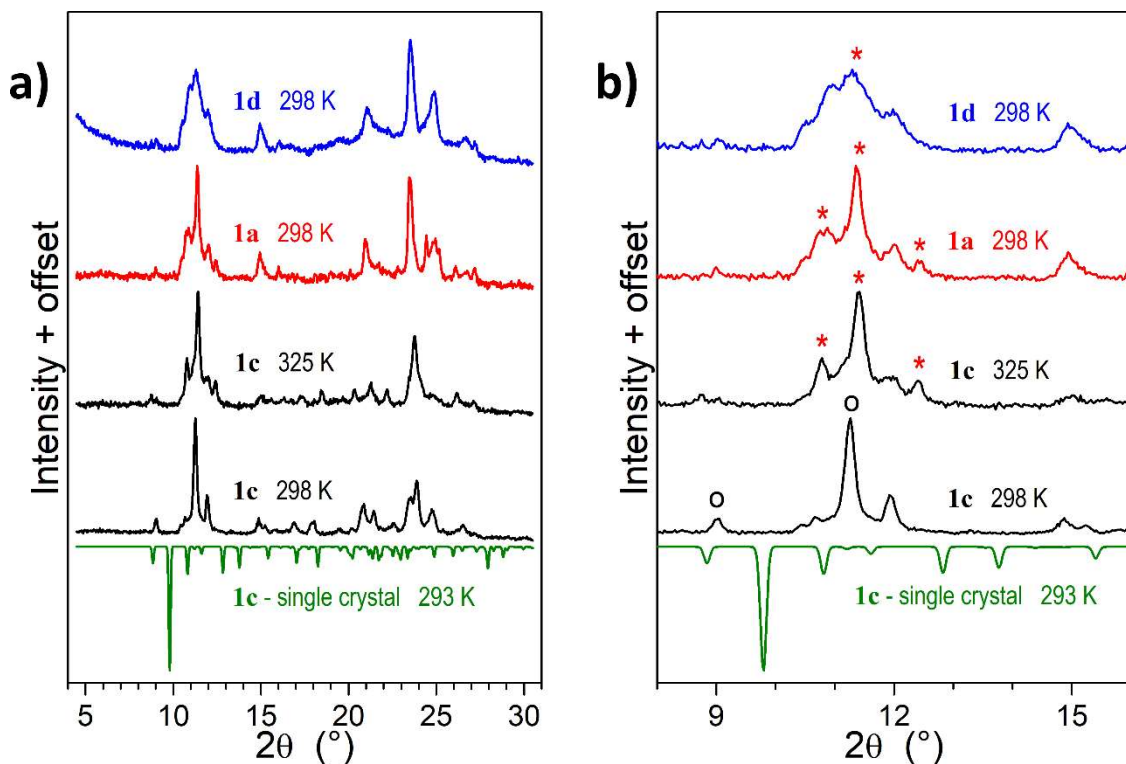


Figure S6. (a) Small- and wide-angle X-ray scattering (SWAXS) patterns of complexes **1c** (crystallized with lattice solvent), **1a** (crystallized without lattice solvent) and **1d** (solvent-free powder), as compared to pattern simulated from single crystal structure of **1c**; (b) expanded portion of (a) in the $2\theta = 8^\circ$ - 16° range; stars and rings point the relevant reflections for comparison. The **1c** crystals used for SC-XRD and SWAXS analysis display different structures presumably because of the modified solvent distribution. After heating, **1c** structure becomes similar to **1a**, revealing the release of the lattice solvent. Solvent-free structures **1a** and **1d** are also similar, the powder sample giving broadened reflections because of the small crystal size.

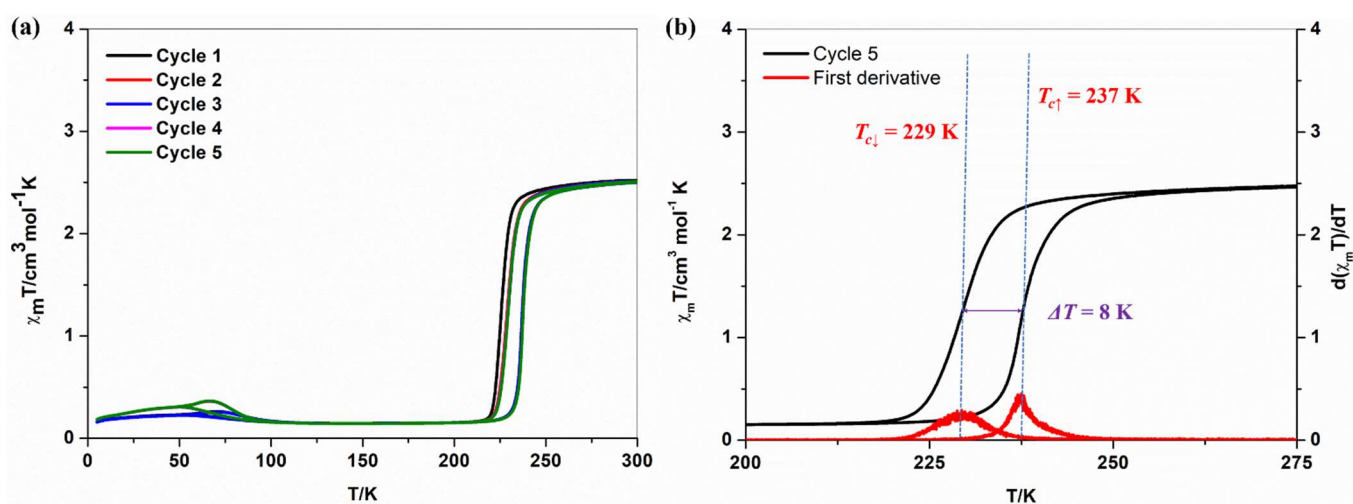


Figure S7. (a) $\chi_m T$ versus T plots, and (b) $d(\chi_m T)/dT$ versus T and $\chi_m T$ versus T plots of complex **1d** corresponding to cycle 5. The critical temperatures (T_c) associated with the cooling and heating branches are designated as $T_{c\downarrow}$ and $T_{c\uparrow}$, respectively.

S6. Differential scanning calorimetry studies of complexes **1c** and **1d**

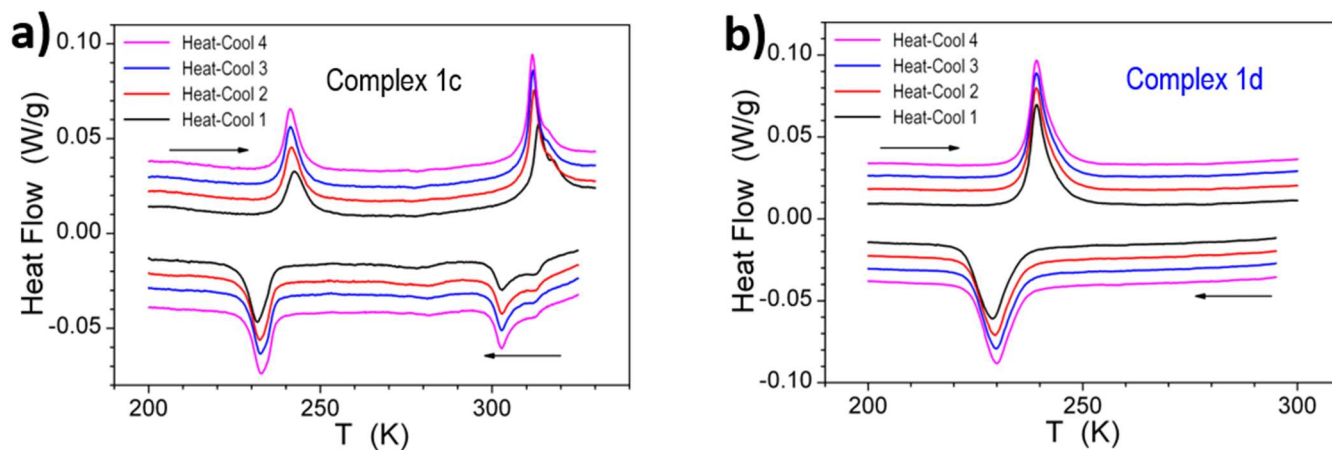


Figure S8. Differential scanning calorimetry (DSC) curves of complexes (a) **1c** and (b) **1d**. A scanning rate of 2 K/min, was employed; endotherm (up).

References

1. "M86-E01078 APEX2 User Manual", Bruker AXS Inc., Madison, USA, 2006.
2. G. M. Sheldrick, *Acta Cryst.* 2008, **A64**, 112-122.
3. R. Pritchard, C. A. Kilner and M. A. Halcrow, *Chem Commun*, 2007, 577–579.